The Use of Strontium Ferrite Perovskite as an Oxygen Carrier in the Chemical Looping Epoxidation of Ethylene

S. Gabra[*1], E. J. Marek[1], S. Poulston[2], G. Williams[2], J. S. Dennis[1].

[1]Department of Chemical Engineering and Biotechnology, University of Cambridge, Philippa Fawcett Drive, CB3 0AS, United Kingdom

[2]Johnson Matthey Technology Centre, Blounts Court Road, Sonning Common, Reading RG4 9NH, UK

Abstract

In the epoxidation of ethylene to ethylene oxide using chemical looping, Ag is supported on strontium ferrite perovskite, where Ag acts as the catalyst while the perovskite acts as an oxygen carrier. This study explores how various oxygen carriers based on strontium ferrite affect chemical looping epoxidation. The structure of the oxygen carrier was varied by incorporating different ratios of two perovskite phases: cubic $SrFeO_3$, and a layered Ruddlesden-Popper (RP) phase: $Sr_3Fe_2O_7$. Maximum yield of ethylene oxide was obtained for the sample with 1:1 $SrFeO_3$:RP ratio, leading to an increase in the yield of ethylene oxide around 4 times, compared to only $SrFeO_3$ (*i.e.* 0.4 to 1.6% ethylene oxide yield). These results confirm a possibility of designing the oxygen carriers used in chemical looping epoxidation towards optimal performance. Such a design approach can be expanded to other chemical looping processes to tune the performance of oxygen carrier for the reaction in question.

Keywords: Epoxidation; Chemical looping; Ethylene oxide; Perovskite; Strontium ferrite

1. Introduction

Chemical looping (CL) depends on conveying lattice oxygen, instead of gaseous oxygen, to a reaction. A metal oxide, termed an oxygen carrier, donates its lattice oxygen to a gaseous reactant, and consequently is reduced to a lower oxidation state of the metal. The reduced oxygen carrier is then withdrawn from the site of this reaction, reoxidised with air, and then recycled to repeat the first step of donating oxygen to the reaction. Such a scheme enables the physical, or temporal, separation between air and the gaseous reactant. In the context of selective oxidation of organic chemicals, the chemical looping approach would eliminate the need for co-feeding gaseous oxygen with the organic substrates. As a result, only the organic component would be fed to a reactor containing the oxygen carrier coupled with a catalyst for the reaction. This represents an important improvement in safety because, in the CL route, there is a minimal risk of creating explosive mixtures (organic components mixed with air). Such improved safety means that dilution of feed gases is no longer necessary, leading to lower separation costs and possible intensification of the process. Additionally, by changing the nature of the oxygen species contributing to the reaction, from adsorbed gaseous oxygen to lattice oxygen, the CL approach might help in increasing the selectivity of multi-reaction processes towards the desired products.

CL has been explored for the production of a number of chemicals, including syngas [1], ethylene [2,3] and ethylene oxide [4]. For these processes, a suitable oxygen carrier must possess several characteristics, such as: (i) sufficient oxygen capacity, (ii) favourable thermodynamics, (iii) the capability to be reoxidised rapidly, (iv) resistance to attrition, melting and agglomeration, and (v) reasonable cost [5]. An *in-silico* screening of suitable materials for CL has revealed that strontium ferrite is a promising oxygen carrier owing to its high stoichiometric oxygen capacity, resistance to carbonation and the ability to withstand many redox cycles [6,7]. Capitalising on these favourable characteristics, Chan *et al.* (2018) explored the feasibility of supporting Ag on $SrFeO_{3-\delta}$ and using the resultant particle as a catalyst for the epoxidation of ethylene in a CL arrangement. The rationale behind using Ag for such catalysts is that the commercial production of ethylene oxides from ethylene already depends on Ag based heterogenous catalysts, where Ag is the active metal. The chemical looping catalyst was active for epoxidation, resulting in 4% conversion of ethylene and 25% selectivity towards ethylene oxide. Such activity is significantly lower than the activity exhibited by industrial catalysts in direct epoxidation with $O_{2(g)}$ (*e.g.* ~ 85% selectivity and 10% ethylene conversion) [8]. Improving the competitiveness of the CL approach will require higher conversions to ethylene oxide. Clearly, the oxygen carrier has an important influence over this, being the

* Corresponding author. Tel: +44 7404 282239
E-mail address: sg788@cam.ac.uk

46 only source of oxygen for the reaction. Indeed, we showed in a recent study that modifying $SrFeO_3$ with ceria led
47 to catalysts with 60% selectivity at 10% conversion of ethylene, representing a significant improvement in
48 performance compared to using $SrFeO_3$ only [9].

49   In the present study we have investigated a mixture of the two perovskite-type phases, $SrFeO_{3-\delta}$ ($0 \leq \delta \leq$
50 0.5) and $Sr_3Fe_2O_{7-\gamma}$ ($0 \leq \gamma \leq 1$) as oxygen carriers. The two phases differ with respect to the crystal structure,
51 chemical potential and solid-state oxygen transport [10]. Depending on oxygen vacancy ordering, the crystal
52 structure of $SrFeO_{3-\delta}$ can be cubic ($\delta = 0$), tetragonal ($\delta = 0.125$), orthorhombic ($\delta = 0.25$) or brownmillerite ($\delta =$
53 0.5) [11]. On the other hand, $Sr_3Fe_2O_{7-\gamma}$ is a Ruddlesden-Popper oxide with a tetragonal structure [12], that uses
54 different pathways for oxygen-ion transport, which give such oxide excellent oxygen transport properties [13].

55   So far, most of the studies focusing on strontium ferrites have used one material alone, *viz.* $SrFeO_{3-\delta}$ [4,14]
56 or $Sr_3Fe_2O_{7-\gamma}$ [15,16]. In this study, we propose a simple preparation method that results in a mixture of the two
57 perovskite phases. The resulting multi-phase materials are then used as oxygen carriers for chemical looping
58 epoxidation of ethylene. We use the experimental results to discuss the feasibility of designing oxygen carriers of
59 tailored properties for epoxidation and specific operating conditions.

60 ## 2. Experimental

61 ### 2.1. Catalyst preparation

62   Here, the word "catalyst" will be used to describe a composite comprising an oxygen carrier and, deposited
63 on its surface, metallic silver. Ruddlesden-Popper ($Sr_3Fe_2O_{7-\gamma}$) and cubic perovskite ($SrFeO_{3-\delta}$) phases will be
64 referred to as 'RP phase' and 'cubic phase', respectively. Using the technique of Chan *et al.* (2018), the catalyst
65 was made in two stages: preparation of the support material (oxygen carrier) followed by the impregnation of the
66 support with silver. The support was synthesised in the solid state by mixing stoichiometric amounts of $SrCO_3$
67 (Sigma Aldrich, $\geq 98\%$) and Fe_2O_3 (Fisher Scientific, $\geq 95\%$), required to obtain a final material with the desired
68 ratio of the cubic phase and the RP phase. Ethanol was added to aid the wet milling of precursors at a level of 0.25
69 $ml/g_{precursors}$. The mixture of $SrCO_3$ and Fe_2O_3 was ball-milled at 25 Hz for 3 h, with manual agitation at hourly
70 intervals to ensure homogeneity. The mixture was then dried in an oven at 50°C for 24 h, and the resulting cake
71 was crushed and sieved to three ranges of particle size: <180, 180-355, and >355 μm. Afterwards, the particles
72 were calcined at 1000°C for 10 h. The particles were sieved again after calcination to 212-300 μm, which was the
73 size fraction used for further preparation of the catalyst.

74   Ag was loaded onto the oxygen carrier particles using incipient wetness impregnation, resulting in a
75 loading of 15 wt%. The impregnation was performed by adding an aqueous solution of $AgNO_3$ ($\geq 99.8\%$, Fisher
76 Scientific) to the perovskite support. The volume of the solution was the same as the volume of pores in the support,
77 which was determined empirically beforehand, by adding water dropwise to the solid particles agitated with a
78 spatula, until the particles started to cohere. In a typical impregnation step, the batches of the catalysts were
79 prepared using 5 g of the oxygen carrier particles, 1.3895 g of $AgNO_3$, and 1.2 mL of de-ionised water. The
80 weighed mass of $AgNO_3$ was dissolved in the prepared volume of water, and the solution was added dropwise to
81 a thin layer of support with a continuous agitation by a spatula. The batch was then dried at 120°C for 12 h and
82 then calcined at 500°C for 5 h.

83   To ensure reproducibility, three batches were prepared for each investigated type of catalyst. Both
84 preparation steps, including the synthesis of the oxygen carrier and the impregnation of Ag, were repeated. The
85 results from the same batch were highly reproducible, so the results reported in this study represent the different
86 batches prepared, rather than replicas of the same batch.

87   Two control samples were prepared to investigate the effect of water on the catalyst. The first sample was
88 prepared by "impregnating" the bare support with just water. This null impregnation was performed by adding 1.2
89 mL of de-ionised water to the particles with intermediate RP content. The control sample, referred to as '$H_2O/50$
90 SFO', was used to investigate the effect of water, in comparison to the aqueous solution of $AgNO_3$. To explore the
91 effect of excess water on the perovskite, a second control sample was prepared by suspending $SrFeO_3$ particles in

a silver solution for 1 hour. The silver solution was prepared by dissolving 1.3895 g of $AgNO_3$ in 100 mL of de-ionised water. The suspended particles were then filtered and dried at 120°C for 12h. The dried particles were analysed using XRD to check their final structure.

2.2. Catalytic performance

The catalysts were investigated in a vertically-mounted, packed-bed reactor, which was heated using high-temperature dual-element heating tape (Omega, DHT052020LD). The heating tape was controlled by a type K thermocouple inserted in the bed, with the junction of the thermocouple located approximately 10 mm from the bottom of the bed. The packed bed consisted of an 8 mm i.d., 200 mm long quartz tube with a sintered disc fixed 75 mm from the bottom. The reactor was filled as follows, from the bottom to the top: 1 g of α-Al_2O_3, 2 g of catalyst, and 3 g of α-Al_2O_3. The ends of the quartz tube were connected to Swagelok Ultra-Torr® vacuum fittings and sealed with fluorocarbon FKM O-rings. The gases were fed from the top of the reactor and the flowrates were controlled with rotameters and checked with an ADM flowmeter (Agilent). An illustrating schematic diagram of the experimental assembly and packed bed reactor is shown in the Supplementary Information (Fig. S1). The reaction was undertaken at 270°C and atmospheric pressure with a feed rate of gas of 200 mL/min (as measured at 293 K, 1 atm). A cycling experiment consisted of reduction, purge and oxidation stages, performed as: (i) t_{red} = 1.5 min reduction with 5.16 vol% C_2H_4, balance N_2, (ii) 2 min purge with N_2, (iii) t_{ox} = 15 min oxidation with air, (iv) 2 min purge with N_2. The importance of the purge stage is to avoid mixing ethylene and air which ensures the absence of any flammable mixtures, in addition to eliminating any cofeeding reactions. The duration and flowrate of N_2 were specified, according to pipeline purging principles, to ensure that the whole system is properly purged [17]. In addition, the experiments were designed to generate low concentrations of EO, compared to the industrial process, for safety reasons. The gases used for the reaction, supplied by BOC, were: 5.16 vol% C_2H_4, balance N_2 (certified to 5% uncertainty), N_2 (purity > 99.998%), and industrial grade air. The product gases from the reactor were analysed using a Fourier-transform infrared (FTIR) analyser (MKS Instruments, MultiGas™ 2030). Each measurement consisted of 8 scans of the band 800 – 4600 cm^{-1}, lasting 4 s, and at a resolution of 0.5 cm^{-1}. The analysis regions of the quantified species were adjusted to ensure the absence of any cross-sensitivities. The quantified species were CO, CO_2, H_2O, C_2H_4, and EO. The mean selectivity towards ethylene oxide (EO) was calculated as:

$$\bar{S} = \frac{\text{Total carbon in EO}}{\text{Total carbon in all products}} = \frac{\int [EO] dt}{\int \left([EO] + \frac{1}{2}[CO_2] + \frac{1}{2}[CO] \right) dt}$$

where [i] is the measured mole fraction of species i, and t is time.

The conversion of ethylene was estimated as:

$$\bar{X} = \frac{\text{Total carbon in all products}}{\text{Total carbon detected}} = \frac{\int [EO] + \frac{1}{2}[CO_2] + \frac{1}{2}[CO] dt}{\int \left([C_2H_4] + [EO] + \frac{1}{2}[CO_2] + \frac{1}{2}[CO] \right) dt}$$

To ensure that there was no accumulation of coke in the reactor, the carbon balance was evaluated using:

$$\text{Carbon balance} = \frac{\text{Total carbon detected}}{\text{Total carbon fed}} = \frac{\int \left([C_2H_4] + [EO] + \frac{1}{2}[CO_2] + \frac{1}{2}[CO] \right) dt}{[C_2H_4]_{feed} \times t_{red}}$$

where $[C_2H_4]_{feed}$ was the mole fraction of C_2H_4 in the feed. For all experiments, the carbon balance was within 95 ± 5%. Finally, the yield of EO was calculated as:

$$\bar{Y} = \bar{X} \times \bar{S}$$

The instantaneous selectivity at time t was calculated as:

$$S(t) = \frac{\text{Concentration of EO}}{\text{Concentration of carbon in products}} = \left.\frac{[EO]}{[EO] + \frac{1}{2}[CO_2] + \frac{1}{2}[CO]}\right|_t$$

130   While the instantaneous conversion at time t was calculated according to:

$$X(t) = \frac{\text{Concentration of carbon in products}}{\text{Concentration of carbon in all species}} = \left.\frac{[EO] + \frac{1}{2}[CO_2] + \frac{1}{2}[CO]}{[C_2H_4] + [EO] + \frac{1}{2}[CO_2] + \frac{1}{2}[CO]}\right|_t$$

131

2.3. Catalyst characterisation

132

133   Scanning electron microscopy (SEM) was performed using a Tescan MIRA3 FEG-SEM to study the
134   surface morphology of the catalysts. Particles were sputter coated with a thin layer of platinum (~10 nm) to
135   eliminate the charging effect caused by non-conductive parts of the sample, hence improving the quality of the
136   images taken. Backscattered-Electron (BSE) imaging was used in parallel with secondary electron (SE) imaging,
137   to visualise the texture at the surface of the catalyst. Elemental analysis of the catalyst's surface was carried out
138   using Energy-dispersive X-ray spectroscopy (EDS), conducted with Oxford Instruments Aztec Energy X-maxN
139   80 EDS.

140   Powder X-ray diffraction (XRD) patterns of the oxygen carrier particles were collected in the $2\theta = 10-90°$
141   range, using an Empyrean PANalytical diffractometer with CuKα radiation. Rietveld refinement was conducted
142   using Maud software to identify the phase composition of the prepared samples [18]. The reference patterns used
143   to identify the phases were ICSD-2648 ($Sr_3Fe_2O_7$), ICSD-91062 ($SrFeO_3$), ICSD-69022 ($SrFe_{12}O_{19}$). The results
144   from the Rietveld analysis for one of the samples is shown in the Supplementary Information (Fig. S2).

145   Thermogravimetric analysis (TGA) was used to characterise thermochemical properties of the prepared
146   oxygen carriers and catalysts, using a TGA/DSC 1, Mettler Toledo analyser. Approximately 30 mg of sample was
147   loaded into a 70 μl alumina crucible and placed on top of a balance arm located in the middle of the TGA chamber.
148   Protective, purge and reactive gas flows were maintained throughout the experiments. The protective and purge
149   flows were composed of Ar (50 mL/min each, measured at 293 K and 1 atm). Either air or ethylene was used as
150   the reactive gas (50 mL/min, measured at 293 K and 1 atm), fed through a capillary tube located above the crucible.

151   Two TGA programmes were used to investigate the oxygen release from the catalysts. The first was
152   conducted in air and involved heating the sample from 50 to 900°C with a heating rate of 10°C/min, and then
153   cooling to 50°C, also in air and with the same rate. This was repeated three times, giving results from three cycles
154   of oxygen release (in heating) and uptake (during cooling). The second TGA programme aimed at investigating
155   the catalytic behaviour and cyclic stability during epoxidation, carried out at 270°C. After reaching the reaction
156   temperature, the program consisted of four steps: (i) purge in N_2 for 2 min, (ii) reduction in 5.16 vol% C_2H_4 in
157   balance N_2 for 20 min, (iii) purge in N_2 for 2 min, and (iv) oxidation in air for 60 min. This was repeated for 4
158   cycles during one continuous experiment.

3. Results

159

3.1. Phase identification and morphology

160

161   Figure 1 shows the XRD patterns for the prepared oxygen carriers, while Table 1 shows the results for the
162   quantitative phase analysis. As planned, the phase composition varied between all prepared samples. For each
163   material, the evaluated composition contained more $Sr_3Fe_2O_{7-\gamma}$ than intended, which is consistent with the
164   observation of Lau *et al.* (2017), that preparing pure $SrFeO_3$ can yield a mixture of $SrFeO_3$ and $Sr_3Fe_2O_{7-\gamma}$. Due to
165   the detection limit of the XRD, the experimental uncertainty translates to ~1-2% uncertainty for analysing the
166   composition in the Rietveld refinement [19]. This value is close to the weight fractions of the minor phase, *i.e.,*
167    $SrFe_{12}O_{19,}$ which in consequence can be discarded. Hereinafter, the samples are denoted x SFO, where x refers to
168   the intended weight fraction of $Sr_3Fe_2O_{7-\gamma}$.
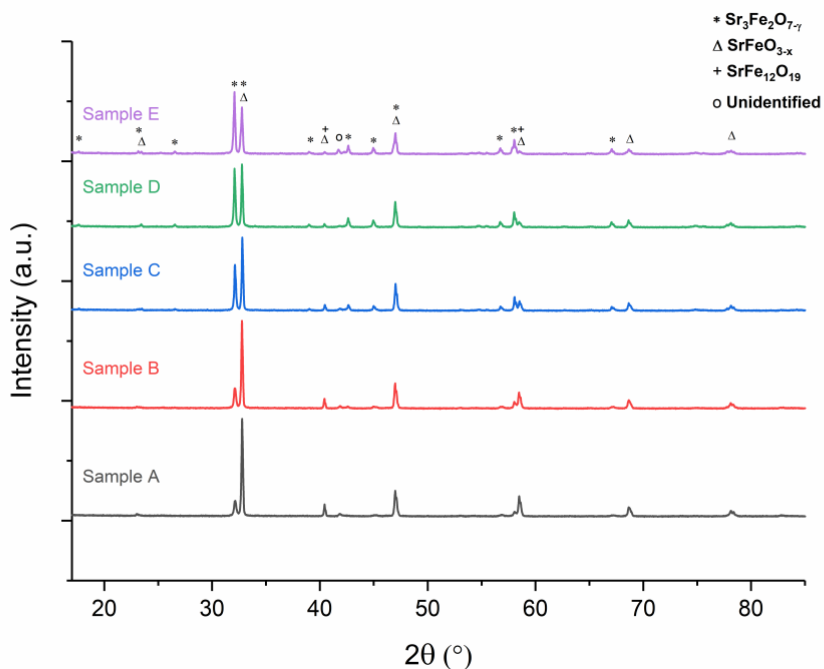
Figure 1 XRD patterns for the five prepared oxygen carriers, with varied ratios of $SrFeO_{3-\delta}$ and $Sr_3Fe_2O_7$. Refer to Table 1 for the compositions.

Table 1 Quantitative phase analysis for five oxygen carriers with varied ratios of $SrFeO_{3-\delta}$ and $Sr_3Fe_2O_7$. The reported values for actual composition are averaged across three batches. The variability was $\pm 2\%$.

	Mole ratio		Intended composition (wt%)		Actual composition (wt%)		
	$SrCO_3$	Fe_2O_3	$SrFeO_{3-\delta}$	$Sr_3Fe_2O_{7-\gamma}$	$SrFeO_{3-\delta}$	$Sr_3Fe_2O_{7-\gamma}$	$SrFe_{12}O_{19}$
Sample A (SFO)	0.72	0.36	100%	0%	75.0%	23.0%	2.0%
Sample B (25 SFO)	0.74	0.34	75%	25%	59.5%	39.0%	1.5%
Sample C (50 SFO)	0.76	0.32	50%	50%	34.0%	65.0%	1.0%
Sample D (75 SFO)	0.79	0.29	25%	75%	17.5%	82.0%	0.5%
Sample E (100 SFO)	0.81	0.27	0%	100%	5.0%	95.0%	0.0%

Energy-dispersive X-ray spectroscopy (EDS) and SEM were used to examine the surface morphology and the distribution of silver on the surface of the catalysts. An example SEM image of Ag/SFO, shown in Fig. 2, presents the typical surface seen in all the prepared catalysts. EDS and SEM images for other samples are shown in the Supplementary Information (Figs. S3 and S4). SEM and EDS images show that the distribution of silver on the surface of the different catalysts is similar, meaning that any discrepancy in catalytic performance between the catalysts is not likely to arise from differences in the presentation of the catalytically active particles of silver. The distribution of silver affects the size of silver particles and exposed surface area of silver and hence might affect catalytic performance [20]. The amount of area covered by silver also influences the amount of exposed surface of the support, which was shown by Chan *et al.* (2018), to be not selective towards EO.
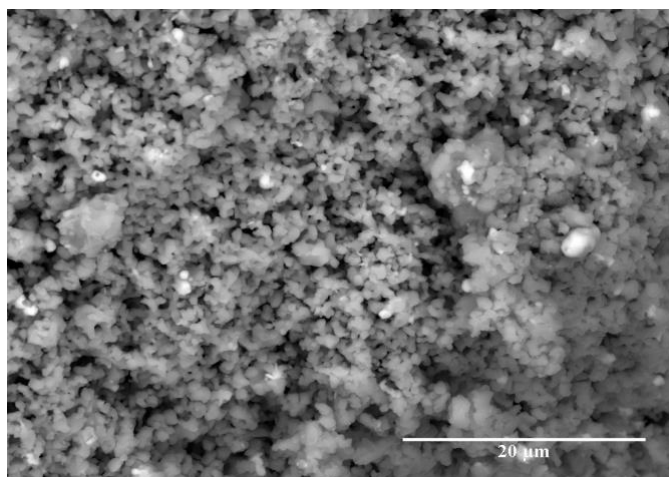
184

185 **Figure 2** SEM image of Ag/SFO. The silver appears as white spherical particles, contrasting with the SFO surface.

186 ### 3.2. Thermogravimetric analysis

187 #### 3.2.1. Temperature-programmed reduction and oxidation in air

188 Figure 3 shows the change in mass of SFO, 50 SFO, and 100 SFO samples during the second cycle of the
189 temperature programme carried out in the TGA in air. The cycling behaviour for all carriers is shown in the
190 Supplementary Information, Fig. S5. As shown in Fig. 3, the three materials had a similar loss of mass at the end
191 of the reduction stage, releasing oxygen equivalent to up to 1.5% of the initial mass. All the samples, except 100
192 SFO, showed a reversible oxygen uptake and release across the heating (reduction) and cooling (oxidation) cycles
193 with an overlap of reduction and oxidation curves. Because of the observed reversibility, weight change
194 corresponded to oxygen uptake and release from the crystal structure.

195 100 SFO showed somewhat different trends in oxidation and reduction than the other materials. Upon
196 heating, the rate of oxygen release from 100 SFO increased sharply at 400°C. During oxidation, a significant
197 increase in relative mass around 350°C indicated a faster oxygen uptake in this temperature range than observed
198 for the other materials. Yet, between 350°C and 900°C, the oxidation of 100 SFO was slower than the rest of the
199 oxygen carriers. These observations are in line with the results of Beppu *et al.* (2017).
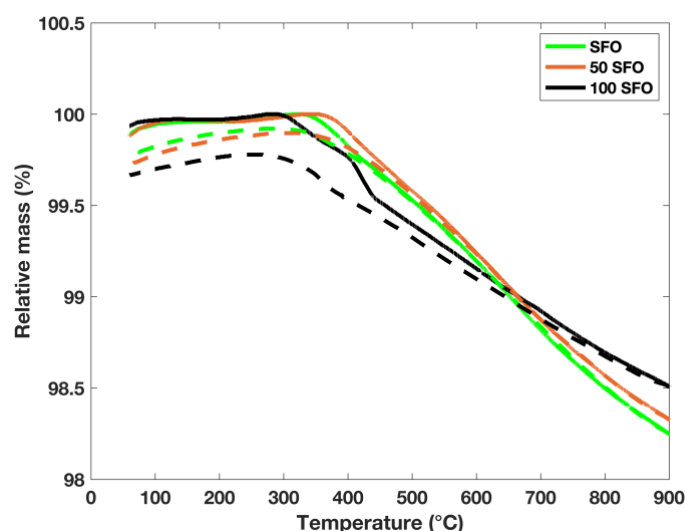
200

201 **Figure 3** Mass change of the different oxygen carriers during a TGA programme in air that included heating from 50 to 900°C and then
202 cooling back to 50°C. The figure shows the normalised mass of the oxygen carrier upon heating (solid line) and cooling (dashed line). The
203 results are for the second of 3 cycles. SFO, 50 SFO and 100 SFO refers to oxygen carriers composed of $SrFeO_3$, 50 wt% $Sr_3Fe_2O_7$ and 100
204 wt% $Sr_3Fe_2O_7$ respectively.

6

The behaviour of silver-impregnated catalysts was also investigated using temperature programmed heating in air. Figure 4 shows the mass change of Ag/50 SFO catalyst compared to bare 50 SFO oxygen carrier. The sample subjected to pure water without $AgNO_3$, *i.e.*, H_2O/50 SFO, is also shown for comparison. The 50 SFO carrier exhibited overlapping oxygen uptake and release trends, where the sample started to lose and gain mass at ~ 400°C. On the other hand, the oxygen release for H_2O/50 SFO and Ag/50 SFO proceeded in three stages: (i) slow release between 300-400°C, (ii) quick release at 400-420°C and (iii) slow release between 420-900°C. Additionally, upon cooling, these two samples exhibited a sharp increase in the oxygen uptake at 350°C. The trends observed for H_2O/50 SFO and Ag/50 SFO were similar to the trends observed for 100 SFO in Fig. 3. For the rest of the investigated catalysts, the results demonstrating oxygen uptake and release are shown in the Supplementary Information, Fig. S6. To check the influence of water on the perovskite structure, bare SFO was suspended in silver solution and the dried powder was analysed using XRD. The XRD patterns, shown in Figure 5, indicate that the suspension of the support particles in the solution led to the evolution of extra phases, including $SrCO_3$ and SrO.
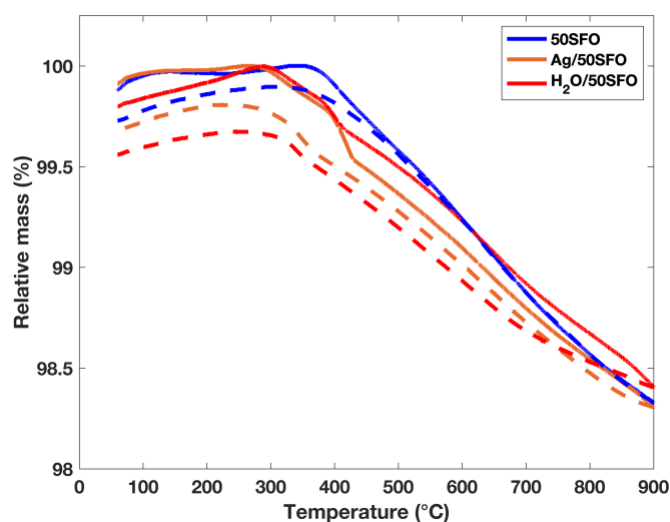
Figure 4 Mass change of 50SFO, H_2O/50SFO, and Ag/50SFO during one cycle in the TGA. The cycle consisted of heating the sample from 50 to 900°C and cooling back to 50°C, both in air. The figure shows the normalised mass of the oxygen carrier upon heating (solid line) and (b) cooling (dashed line). SFO, 50 SFO and 100 SFO refer to oxygen carriers composed of $SrFeO_3$, 50 wt% $Sr_3Fe_2O_7$ and 100 wt% $Sr_3Fe_2O_7$, respectively.
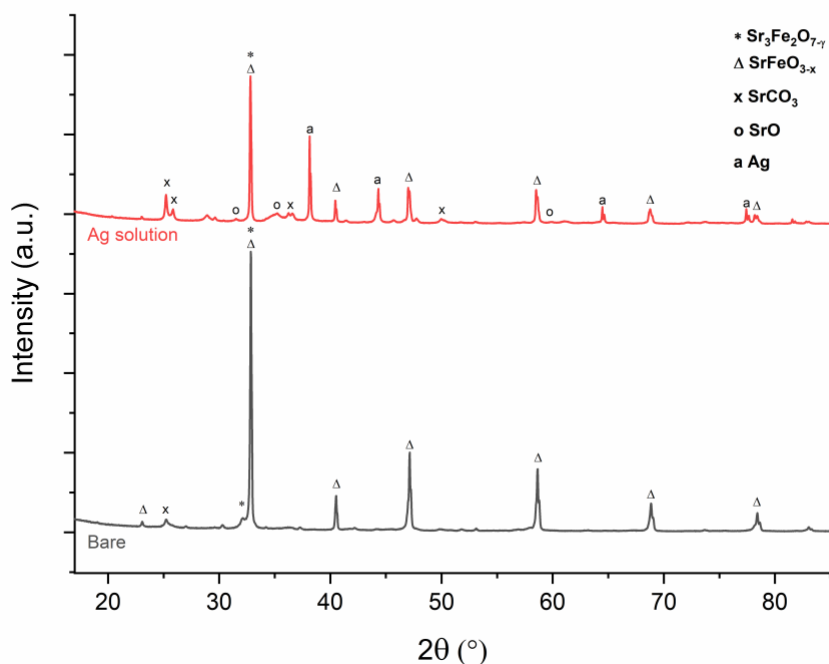
Figure 5 XRD patterns for bare SrFeO$_3$ (black) and SrFeO$_3$ suspended in silver solution (red).

3.2.2. Isothermal reduction in ethylene

Figure 6 shows the change in mass of the prepared catalysts (Ag + oxygen carrier) during an epoxidation cycle at 270°C in the TGA. Looking at the initial rates of oxygen release for the different samples, Ag/100 SFO experienced the fastest release of oxygen, followed by Ag/50 SFO, and finally Ag/SFO. Eventually, all three catalysts reduced to a similar level upon the 20 min epoxidation-step in the TGA. During subsequent oxidation, the catalysts with a high fraction of the RP phase oxidised much quicker than the sample predominantly composed of SrFeO$_3$. For example, in the first 15 minutes of oxidation 100 SFO was able to regain ~ 85% of the mass lost in reduction, compared to only ~ 26% for SFO. The importance of reoxidation was investigated by Chan *et al*. (2018), who noticed that longer time of oxidation improves the activity and selectivity of Ag/SFO.

The cyclic stability of catalysts was investigated by comparing the mass change in four cycles of epoxidation. Cycle 1 is not discussed as this cycle exhibited significantly different patterns of mass loss compared to the other cycles. The first cycle typically involves the removal of impurities deposited on the sample during storage [6,7]. Table 2 shows the change in the amount of released oxygen between the second and fourth cycle, while graphs showing the change in mass for the different catalysts across the cycles can be found in the Supplementary Information, Fig. S7. Samples with low ratios of the RP phase released less oxygen in subsequent cycles, compared to samples with a high RP phase content, which also gave significantly more stable results across the redox cycles. The rates of oxygen release for the three samples can be found in the Supplementary Information, Fig. S8.

Table 2 Change in the amount of oxygen released by different catalysts during cycling experiments at 270°C in the TGA. The results indicate the change between the second and fourth cycles.

| Sample	Change in released oxygen (%)
A (Ag/SFO)	-16.19
C (Ag/50 SFO)	-10.17
E (Ag/100 SFO)	-0.58
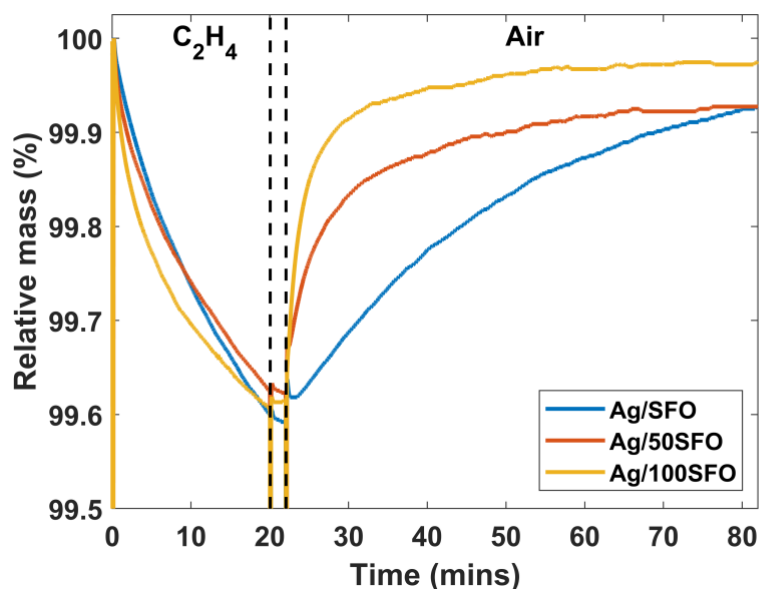
Figure 6 Mass change during oxidation and reduction of prepared catalysts during an epoxidation cycle, carried out at 270°C in the TGA. The presented cycle consisted of 20 min reduction in ethylene, 2 min purge in N_2, and 60 min oxidation in air. The shown trends are for the second of 4 subsequent cycles. SFO, 50 SFO and 100 SFO refer to oxygen carriers composed of $SrFeO_3$, 50 wt% $Sr_3Fe_2O_7$ and 100 wt% $Sr_3Fe_2O_7$, respectively.

3.3. Catalytic performance in packed bed

The different oxygen carriers, loaded with silver, were investigated in a chemical looping mode in a packed-bed reactor. Figure 7 shows example profiles of product EO and CO_2 for Ag/50 SFO collected over 5 redox cycles. As indicated earlier, the reduction step lasted for 1.5 min, during which EO and CO_2 were detected. The highest concentrations of EO and CO_2 were observed in the first cycle. Afterwards the activity decayed and then stabilised after the third cycle.
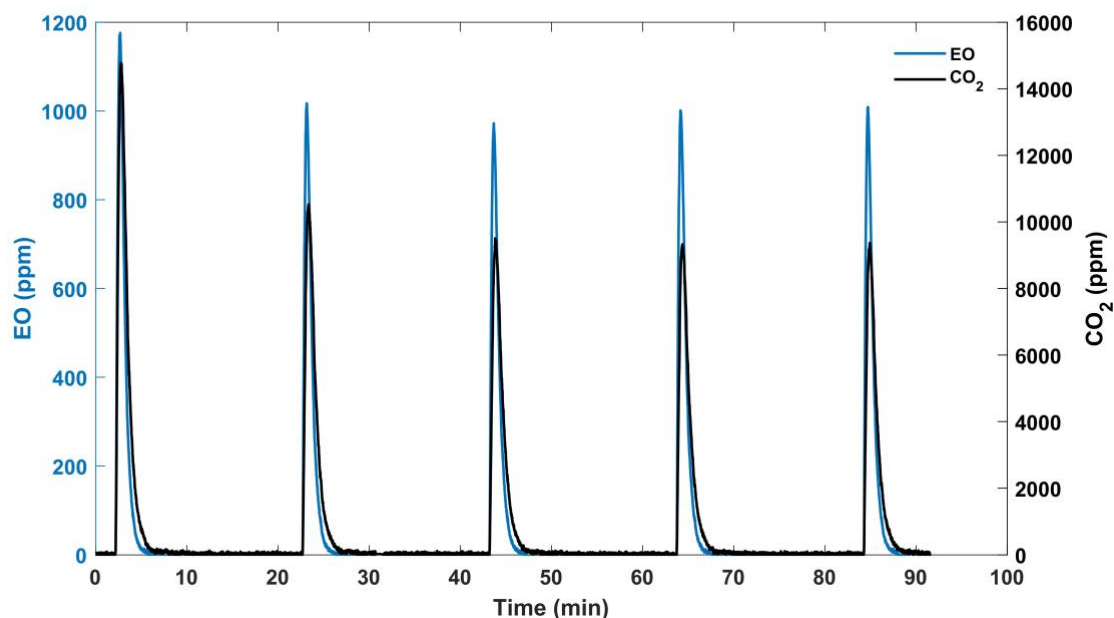

Figure 7 Concentration of ethylene oxide (EO) and CO_2 measured during five epoxidation cycles in experiments carried out in a packed bed. The catalyst used for this experiment was Ag/50 SFO. Conditions: 270°C, 1 atm, 2 g of catalyst, feed of 200 mL/min (as measured at 293 K, 1 atm). Cycling times: (i) t_{red} = 1.5 min reduction with 5.16 vol% C_2H_4 in balance N_2, (ii) 2 min purge with N_2, (iii) t_{ox} = 15 min oxidation with air, and (iv) 2 min purge with N_2.

9

Figure 8 shows results for selectivity, conversion and yield obtained during five epoxidation cycles for three catalysts. The error bars represent the maximum, minimum and mean from three repeats. The results for all the samples are shown in the Supplementary Information, Fig. S9. The results indicate that with increasing proportion of RP phase in the catalyst, the initial selectivity towards EO decreases from ~20% to 10%. However, the selectivity was more stable against cycling when RP phase was present in the oxygen carrier, while for the samples based on SFO, the selectivity decreased across cycles. For example, the selectivity of SFO, decayed from around 20% in the first cycle to 15% in the fifth cycle. In contrast, the mean selectivity of 50 SFO, increased from 11% to 16%. This increase resulted mainly from a decrease of CO_2 concentration in the product gases, while the concentration of EO remained at a similar level, which can be observed by analysing the concentration profiles in Fig. 7. On the other hand, the catalysts with an intermediate proportion of the RP phase exhibited the highest conversion levels compared to the catalysts with the high or low RP phase content. For example, in the last cycle SFO and 50 SFO resulted in conversion between 3 and 5%, while 50 SFO resulted in conversion of ~ 10%. Consequently, the highest yield for EO was obtained for 50 SFO catalyst, reaching around 1.6% in the last cycle. This represents an increase of around four times compared to the yield from experiments with SFO and 100 SFO catalysts.


(a)

(b)

(c)
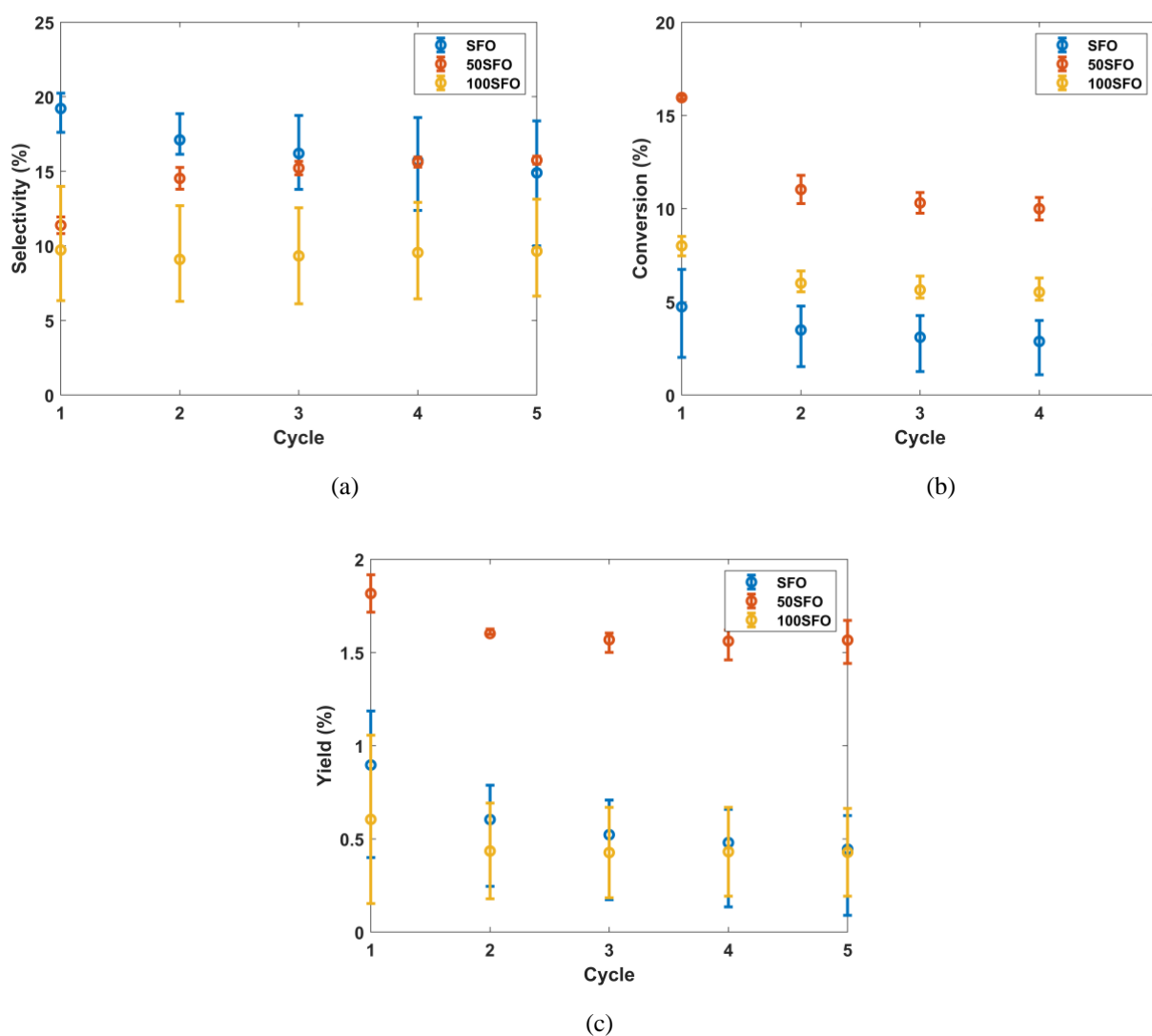
Figure 8 (a) Selectivity towards EO, (b) conversion of C_2H_4, and (c) yield of EO for various catalysts, obtained during chemical looping epoxidation, carried out in the packed bed. SFO, 50 SFO and 100 SFO refer to oxygen carriers composed of $SrFeO_3$, 50 wt% $Sr_3Fe_2O_7$ and 100 wt% $Sr_3Fe_2O_7$, respectively.

Figure 9 shows the variation of instantaneous selectivity and conversion for the different catalysts as a function of the amount of oxygen released in packed bed experiments. As shown, the instantaneous selectivity for all catalysts drops as the oxygen content of the carrier progressively falls. The decay in selectivity is less

pronounced in the catalysts with a larger proportion of the RP phase, with 100 SFO catalyst experiencing the slowest decay. Similarly, the instantaneous conversion for all catalysts drops throughout the reduction step. However, the decay in conversion is more pronounced in the catalysts rich in the RP phase, with 100 SFO experiencing the steepest decay. As shown in Fig. S10 in the Supplementary Information, the amount of oxygen released from the presented samples was steady across the reduction stage, with 50 SFO releasing the highest total amount of oxygen, followed by 100 SFO and finally SFO.

(a)   (b)
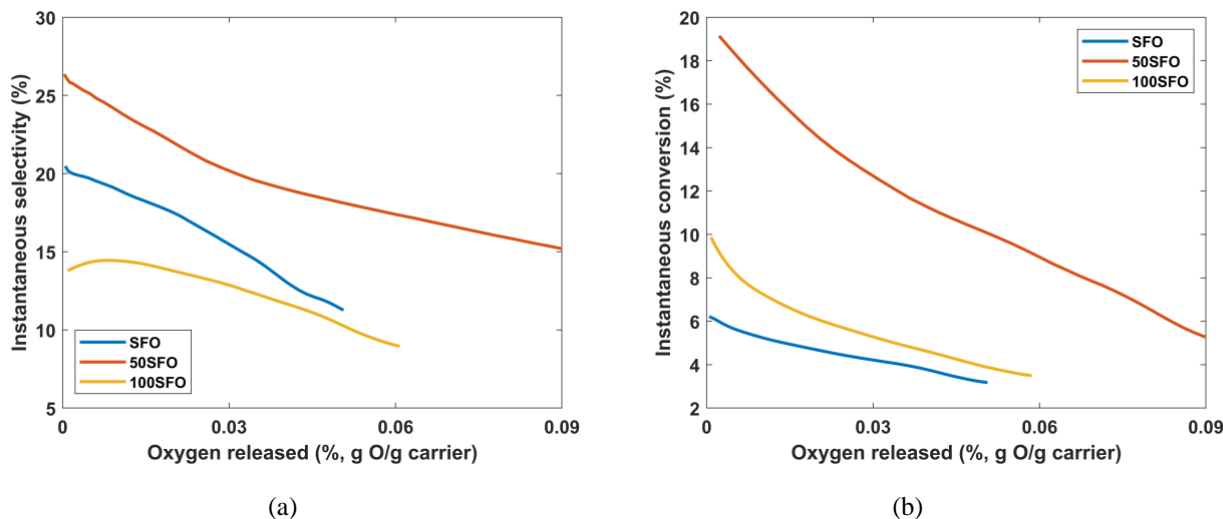
Figure 9 Variation of instantaneous (a) selectivity, and (b) conversion for different catalysts in respect to the amount of released oxygen (based on the products, EO and CO_2) during experiments in packed bed. The curves represent average results from cycles 2-4. SFO, 50 SFO and 100 SFO refer to oxygen carriers composed of $SrFeO_3$, 50 wt% $Sr_3Fe_2O_7$ and 100 wt% $Sr_3Fe_2O_7$, respectively.

4. Discussion
4.1. Characterisation of oxygen carriers

Figures 3 and 4 show the results of a temperature-programmed reduction and oxidation in air for the prepared materials. The results describe the basic thermochemical properties of these oxygen carriers. Overall, all carriers released similar amounts of oxygen upon heating to 900°C, with SFO showing marginally higher amounts of oxygen released compared to 50 SFO and 100 SFO. At 900°C, the amount of oxygen released for all perovskites is linked to their respective oxygen capacities, since the reaction was limited by equilibrium rather than kinetics at the TGA conditions used [6,21]. Therefore, the available oxygen capacity of both perovskites is important with respect to the amount of oxygen released during the epoxidation experiments, and hence the overall catalytic performance. The oxygen capacity of strontium ferrites depends on their non-stoichiometry. The oxygen non-stoichiometry of $SrFeO_{3-\delta}$ varies in the range $0 \le \delta \le 0.5$ ($SrFeO_{2.5} \leftrightarrows SrFeO_3$), while γ for $Sr_3Fe_2O_{7-\gamma}$ varies between 0 and 1 ($Sr_3Fe_2O_7 \leftrightarrows Sr_3Fe_2O_6$) [10]. In practice, both materials synthesised in air ($pO_2 = 0.21$) will most probably have starting stoichiometries of $SrFeO_{2.82}$ [6] and $Sr_3Fe_2O_{6.75}$ [22] at room temperature. Were the two perovskites to be reduced completely, the oxygen capacities of $SrFeO_{2.82}$ and $Sr_3Fe_2O_{6.75}$ would be 2.71% and 2.49% respectively. This is in line with the experimental results of Beppu *et al.* (2015) that $SrFeO_3$ has a higher oxygen capacity than $Sr_3Fe_2O_7$. For the experiments conducted here, all carriers lost ~1.5% of their starting mass, as the experiments were conducted in an oxidising environment at relatively low temperatures. Mixing the two perovskite phases (*i.e.* $SrFeO_3$ and $Sr_3Fe_2O_7$) should result in a final material that possessed properties proportional to the ratio of the two phases. Indeed, TGA results (Fig. 3) showed that the amount of oxygen released by 50 SFO lies between SFO and 100 SFO. However, the amount of oxygen released is not exactly proportional to the phase ratio of 50 SFO (*i.e.* the oxygen released by 50 SFO is not an average of the two composing phases), since the amount of oxygen released in the TPR experiments depended also on the temperature at which oxygen release started.

Figure 4 shows that the impregnation of the perovskite support with water led to different trends in reduction and oxidation compared to bare support. These trends can be explained by analysing the change in $SrFeO_3$ structure induced by suspension in water. As shown in Figure 5, the suspension of the perovskite in water

11

325 led to the evolution of extra phases, including $SrCO_3$ and SrO. The formation of carbonate species on the surface
326 of the support will lead to a Sr-deficient structure in the perovskite, causing a change in the oxygen uptake and
327 release [23]. The similarity in oxygen release (Fig. 4) between the water-impregnated and $Sr_3Fe_2O_7$-rich samples
328 can be related to the susceptibility of these samples to carbonation. Similar to water-impregnated samples, the
329 $Sr_3Fe_2O_7$-rich samples are more prone to carbonation compared to $SrFeO_3$. This is indicated by the relatively
330 significant mass loss experienced by $Sr_3Fe_2O_7$-rich samples during the first TGA cycle (Supplementary
331 Information, Table S1). This is also in line with the results of Lau *et al.* (2017) who showed that the increase in
332 $Sr_3Fe_2O_7$ weight fraction led to the formation of bigger amounts of carbonates.

333 Besides the amount of available oxygen, the performance in epoxidation may be strongly connected to the
334 rate of oxygen release. Among the prepared materials, the catalysts with high fractions of RP phase exhibited the
335 fastest rates of oxygen release at the start of the reduction stage, as observed in the isothermal experiments in the
336 TGA with C_2H_4 where the observed mass change was limited by slow kinetics (Supplementary Information, Fig.
337 S8). In the same experiments, SFO exhibited the reverse trend, where the rate of oxygen release was initially slow
338 but relatively constant across the reduction stage. The fast reduction of oxygen carriers with high fractions of RP
339 is in line with the observations of Beppu *et al.* (2015) that at low temperatures ($< 500°C$) $Sr_3Fe_2O_7$ reduces faster
340 than $SrFeO_3$. The cause for the fast oxygen transport of RP phase is its crystal structure, which is composed of two
341 perovskite layers ($SrFeO_3$) sandwiching a rock salt layer (SrO) [13]. Such a structure enables rapid migration of
342 interstitial oxygen between the layers, resulting in a high oxygen-ion conductivity [13,24]. The rate of oxygen
343 release in the perovskites depends on δ, representing the oxygen non-stoichiometry of the material [25]. In other
344 words, the rate of oxygen release is expected to decrease as δ gradually increases when the perovskite is reduced.
345 Since 100 SFO initially reduced the fastest, one can expect a lower rate of oxygen release towards the end of the
346 epoxidation step. This was confirmed by the experimental results from the TGA (Supplementary Information, Fig.
347 S8). The combination of two factors: the oxygen capacity of the material, and the rate of oxygen release, is expected
348 to influence the performance of the oxygen carrier in chemical looping epoxidation.

4.2. Catalytic performance

350 For conventional epoxidation, the selectivity towards EO depends on the nature and amount of oxygen
351 present on the catalyst surface [26]. Electrophilic oxygen species are believed to participate in a direct route for
352 EO formation following the Eley-Rideal mechanism, while nucleophilic species and oxygen vacancies are
353 associated with the formation of the oxometallacycle following a Langmuir-Hinshelwood mechanism [27]. The
354 oxometallacycle is a common precursor for both EO and acetaldehyde, being an unstable intermediate,
355 subsequently oxidising to CO_2 and H_2O [28]. From the two types of the involved adsorbed oxygen species, the
356 selective electrophilic species are believed to exist at a highly oxidised Ag surface [27]. Accordingly, an increase
357 in the pressure of the oxygen feed would enhance selectivity towards EO in the conventional co-feeding process
358 [29]. Previous reports and DFT studies have indicated that higher pO_2 increases the concentration of subsurface
359 oxygen, leading to an overall enhancement of EO selectivity [30].

360 For chemical looping epoxidation, the mechanism discussed by Chan *et al.* (2018) suggested that the lattice
361 oxygen in the oxygen carrier is supplied to Ag as subsurface oxygen where this oxygen could further diffuse across
362 Ag to be presented to ethylene as adatom oxygen. Based on their results, Chan *et al.* (2018) assumed that a decay
363 in the concentration of the subsurface oxygen would lead to a decay of the catalytic performance in the chemical
364 looping setup. In conventional co-feeding mode, Jankowiak and Barteau (2005) also showed that the lower level
365 of subsurface oxygen will lead to a decay in the catalytic performance. This is further supported by the results
366 presented in Fig. 9, where the instantaneous selectivity and conversion for all catalysts dropped as the oxygen
367 carriers were progressively reduced. Such trends suggest that it would be profitable to decrease the duration of the
368 reduction stage to maintain high selectivity and conversion levels in the chemical looping arrangement.

369 The high conversion experienced by 50 SFO compared to SFO and 100 SFO might be linked to the mix
370 of properties from the two perovskites, as explained before. 100 SFO released oxygen faster; however, 100 SFO
371 has limited oxygen capacity and was more prone to carbonation compared to SFO. All these factors indicate that
372 samples with pure phases are not optimal and only oxygen carriers with intermediate perovskite ratios are expected

to exhibit favourable catalytic performances, where the two perovskite phases induce a synergistic effect in the production of EO. This is clear by observing the high selectivity, high conversion and high EO yield exhibited by 50 SFO during epoxidation experiments in packed bed (Fig. 8).

For the samples with an intermediate content of the RP phase, the selectivity increased with the number of cycles. Such a trend can be explored by examining the relative amounts of EO and CO_2 produced (Fig. 6). As shown, the levels of EO remained roughly constant across cycles, while CO_2 concentration decreased gradually to almost a steady state. This observation can have two possible explanations, either (i) the catalyst requires an induction period to become more selective, or (ii) contaminants deposited on the surface during storage were gradually removed. Regarding (i), under reaction conditions, silver particles tend to sinter and form larger agglomerates, which are reported to be more active for ethylene epoxidation [31]. However, this increase in particle size due to sintering under reaction conditions does not significantly influence selectivity [31]. In addition, the catalyst did not show increasing levels of EO production across cycles rendering explanation (i) unlikely. The gradual removal of contaminants is possible, since the TGA analysis has confirmed the presence of contaminants (Supporting Information, Fig S6). However, further experiments are required to confirm such mechanism. SFO showed decreasing, rather than increasing selectivity. This indicates that the decrease in selectivity caused by the decaying catalyst stability is more prominent than the increase in selectivity caused by the gradual removal of contaminants. On the other hand, 100 SFO showed relatively constant selectivity. This might be due to that 100 SFO is more prone to carbonation, compromising the decarbonation that happens during the cycle.

The sample with the least amount of the RP phase showed decaying activity across cycles (Fig. 8). This decay was associated with a decrease in the amount of released oxygen, as confirmed by the TGA experiments and summarised in Table 2. In contrast, the catalysts with high fractions of the RP phase exhibited a stable performance over the redox cycles. These trends are correlated with the oxygen uptake rates shown in Figure 6. Samples with a high content of the RP phase oxidised quickly, recovering most of the oxygen that has been lost in the reduction stage. On the other hand, samples with low share of the RP phase did not fully regenerate, gradually losing the available oxygen over time, leading to a decrease in catalytic performance. This would confirm that the amount of available oxygen in the oxygen carrier directly influences its performance during epoxidation.

Overall, the highest initial selectivity was exhibited by the samples with a low content of the RP phase, while samples with the high RP content resulted in high conversion and stable performance in the cyclic operations. However, maximum yields of ethylene oxide were obtained for samples with intermediate perovskite ratios. These samples possessed a mix of favourable properties from the two perovskite phases, $SrFeO_3$ and $Sr_3Fe_2O_7$, including quick oxygen uptake and release, and cyclic stability typical for $Sr_3Fe_2O_7$, as well as high oxygen capacity, characteristic of $SrFeO_3$.

5. Conclusions

This study proposes using different phase ratios of strontium ferrite as oxygen carriers for chemical looping epoxidation of ethylene. The different perovskite phase ratios induced a change in oxygen uptake and release patterns, due to the ability of the two mixed perovskites, $SrFeO_3$ and Sr_3FeO_7, to exhibit multiple stoichiometries and oxygen capacities. This ultimately led to different behaviours in catalytic performances for ethylene epoxidation in chemical looping mode. The results showed that pure perovskite phases are not optimal and only oxygen carriers with intermediate perovskite ratios are expected to exhibit favourable catalytic performances, where the two perovskite phases induce a synergistic effect in the production of EO. The catalytic experiments indicated that 1:1 $SrFeO_3$:RP ratio caused an increase in EO yield of 4-fold (*i.e.* 0.4 to 1.6% ethylene oxide yield) compared to depending solely on $SrFeO_3$. Further research can focus on identifying the optimum perovskite ratio for chemical looping epoxidation. In general, the findings of this study point out to the possibility of designing the oxygen carriers used in chemical looping epoxidation towards optimal performance, in terms of stability and yield of ethylene oxide. Such design approach can be expanded to other chemical looping processes to tune the performance of oxygen carrier for the reaction in question.

6. Acknowledgements

References

[1]   M. Rydén, A. Lyngfelt, Using steam reforming to produce hydrogen with carbon dioxide capture by chemical-looping combustion, Int. J. Hydrogen Energy. 31 (2006) 1271–1283. https://doi.org/10.1016/J.IJHYDENE.2005.12.003.

[2]   S. Al-Ghamdi, M. Volpe, M.M. Hossain, H. de Lasa, VOx/c-Al2O3 catalyst for oxidative dehydrogenation of ethane to ethylene: Desorption kinetics and catalytic activity, Appl. Catal. A Gen. 450 (2013) 120–130. https://doi.org/10.1016/J.APCATA.2012.10.007.

[3]   L.M. Neal, S. Yusuf, J.A. Sofranko, F. Li, Oxidative Dehydrogenation of Ethane: A Chemical Looping Approach, Energy Technol. 4 (2016) 1200–1208. https://doi.org/10.1002/ente.201600074.

[4]   M.S.C. Chan, E. Marek, S.A. Scott, J.S. Dennis, Chemical looping epoxidation, J. Catal. 359 (2018) 1–7. https://doi.org/10.1016/j.jcat.2017.12.030.

[5]   J. Adanez, A. Abad, F. Garcia-Labiano, P. Gayan, L.F. de Diego, Progress in Chemical-Looping Combustion and Reforming technologies, Prog. Energy Combust. Sci. 38 (2012) 215–282. https://doi.org/10.1016/J.PECS.2011.09.001.

[6]   E. Marek, W. Hu, M. Gaultois, C.P. Grey, S.A. Scott, The use of strontium ferrite in chemical looping systems, Appl. Energy. 223 (2018) 369–382. https://doi.org/10.1016/J.APENERGY.2018.04.090.

[7]   C.Y. Lau, M.T. Dunstan, W. Hu, C.P. Grey, S.A. Scott, Large scale in silico screening of materials for carbon capture through chemical looping, Energy Environ. Sci. 10 (2017) 818–831. https://doi.org/10.1039/C6EE02763F.

[8]   S. Rebsdat, D. Mayer, Ethylene Oxide, in: Ullmann's Encycl. Ind. Chem., Wiley-VCH Verlag GmbH & Co. KGaA, 2000.

[9]   E.J. Marek, S. Gabra, J.S. Dennis, S.A. Scott, High selectivity epoxidation of ethylene in chemical looping setup, Appl. Catal. B Environ. 262 (2020) 118216. https://doi.org/10.1016/j.apcatb.2019.118216.

[10]   V. Damljanovic, Raman scattering, magnetization and magnetotransport study of SrFeO3, Sr3Fe2O7 and CaFeO3, University of Stuttgart, 2008. https://doi.org/10.18419/opus-6680.

[11]   Y. Takeda, K. Kanno, T. Takada, O. Yamamoto, M. Takano, N. Nakayama, Y. Bando, Phase relation in the oxygen nonstoichiometric system, SrFeOx (2.5 ≤ x ≤ 3.0), J. Solid State Chem. 63 (1986) 237–249. https://doi.org/10.1016/0022-4596(86)90174-X.

[12]   B. V. Beznosikov, K.S. Aleksandrov, Perovskite-like crystals of the Ruddlesden-Popper series, Crystallogr. Reports. 45 (2000) 792–798. https://doi.org/10.1134/1.1312923.

[13]   Y. Ling, F. Wang, R.A. Budiman, T. Nakamura, K. Amezawa, Oxygen nonstoichiometry, the defect equilibrium model and thermodynamic quantities of the Ruddlesden–Popper oxide Sr 3Fe2O7−δ, Phys. Chem. Chem. Phys. 17 (2015) 7489–7497. https://doi.org/10.1039/C4CP05719H.

[14]   H.X. Dai, C.F. Ng, C.T. Au, The catalytic performance and characterization of a durable perovskite-type chloro-oxide SrFeO3–δClσ catalyst selective for the oxidative dehydrogenation of ethane, Catal. Letters. 57 (1999) 115–120. https://doi.org/10.1023/A:1019091414588.

[15]   T. Ishihara, Y. Shinmyo, K. Goto, N. Nishiyama, H. Iwakuni, H. Matsumoto, NO Decomposition on Ruddlesden–Popper-Type Oxide, Sr 3 Fe 2 O 7 , Doped with Ba and Zr, Chem. Lett. 37 (2008) 318–319. https://doi.org/10.1246/cl.2008.318.

[16]   T. Takashima, K. Ishikawa, H. Irie, Thermal Activiation of Sr3Fe2O7 Electrocatalysts for Water Oxidation at Neutral pH, ECS Trans. 61 (2014) 35–41. https://doi.org/10.1149/06122.0035ecst.

[17]   J.E. Johnson, S.J. Svedeman, C.A. Kuhl, J.G. Gregor, A.K. Lambeth, Pipeline purging principles and practice, in: Proc. Int. Pipeline Conf. IPC, ASME, 1996: pp. 765–775. https://doi.org/10.1115/ipc1996-1882.

[18]   L. Lutterotti, H. Wenk, S. Matthies, MAUD (Material Analysis Using Diffraction): a user friendly Java program for Rietveld Texture Analysis and more, 2 (1999) 1599–1604.

[19]   ITWG, ITWG Guideline on Powder X-Ray Diffraction (XRD) —General Overview, 2015. http://www.nf-itwg.org/pdfs/ITWG-INFL-PXRD.pdf (accessed January 30, 2020).

[20]   J. Lu, J.J. Bravo-Suárez, A. Takahashi, M. Haruta, S.T. Oyama, In situ UV–vis studies of the effect of particle size on the epoxidation of ethylene and propylene on supported silver catalysts with molecular oxygen, J. Catal. 232 (2005) 85–95. https://doi.org/10.1016/J.JCAT.2005.02.013.

[21]   K. Beppu, S. Hosokawa, T. Shibano, A. Demizu, K. Kato, K. Wada, H. Asakura, K. Teramura, T. Tanaka, Enhanced oxygen-release/storage properties of Pd-loaded $Sr_3Fe_2O_{7-\delta}$, Phys. Chem. Chem. Phys. 19 (2017) 14107–14113. https://doi.org/10.1039/C7CP01614J.

[22]   K. Beppu, S. Hosokawa, K. Teramura, T. Tanaka, Oxygen storage capacity of $Sr3Fe2O7-\delta$ having high structural stability, J. Mater. Chem. A. 3 (2015) 13540–13545. https://doi.org/10.1039/C5TA01588J.

[23]   A. Fossdal, M.A. Einarsrud, T. Grande, Phase equilibria in the pseudo-binary system SrO-Fe2O 3, J. Solid State Chem. 177 (2004) 2933–2942. https://doi.org/10.1016/j.jssc.2004.05.007.

[24]   Y. Ling, T. Guo, X. Zhang, R.A. Budiman, Y. Fujimaki, T. Nakamura, B. Lin, T. Kawada, K. Amezawa, Evaluation of electrical conductivity and oxygen diffusivity of the typical Ruddlesden-Popper oxide $Sr3Fe2O7-\delta$, Ceram. Int. 43 (2017) 16264–16269. https://doi.org/10.1016/J.CERAMINT.2017.08.211.

[25]   R.H. Görke, E.J. Marek, F. Donat, S.A. Scott, Reduction and oxidation behavior of strontium perovskites for chemical looping air separation, Int. J. Greenh. Gas Control. 94 (2020) 102891. https://doi.org/10.1016/j.ijggc.2019.102891.

[26]   S. Linic, M.A. Barteau, Construction of a reaction coordinate and a microkinetic model for ethylene epoxidation on silver from DFT calculations and surface science experiments, J. Catal. 214 (2003) 200–212. https://doi.org/10.1016/S0021-9517(02)00156-2.

[27]   M.O. Özbek, R.A. van Santen, The Mechanism of Ethylene Epoxidation Catalysis, Catal. Letters. 143 (2013) 131–141. https://doi.org/10.1007/s10562-012-0957-3.

[28]   S. Linic, M.A. Barteau, Formation of a stable surface oxametallacycle that produces ethylene oxide, J. Am. Chem. Soc. 124 (2002) 310–317. https://doi.org/10.1021/ja0118136.

[29]   J.T. Jankowiak, M.A. Barteau, Ethylene epoxidation over silver and copper–silver bimetallic catalysts: I. Kinetics and selectivity, J. Catal. 236 (2005) 366–378. https://doi.org/10.1016/J.JCAT.2005.10.018.

[30]   Y. Xu, J. Greeley, M. Mavrikakis, Effect of subsurface oxygen on the reactivity of the Ag(111) surface, J. Am. Chem. Soc. 127 (2005) 12823–12827. https://doi.org/10.1021/ja043727m.

[31]   J.E. van den Reijen, S. Kanungo, T.A.J. Welling, M. Versluijs-Helder, T.A. Nijhuis, K.P. de Jong, P.E. de Jongh, Preparation and particle size effects of Ag/A-Al2O3 catalysts for ethylene epoxidation, J. Catal. 356 (2017) 65–74. https://doi.org/http://dx.doi.org/10.1016/j.jcat.2017.10.001.